Chapter 9

Modal Analysis of Surface Plasmon Resonance Sensor Coupled to Periodic Array of Core-Shell Metallic Nanoparticles

Nadson Welkson Pereira de Souza,
Jefferson Souza Costa, Rafael Correa dos Santos,
André Felipe Souza da Cruz,
Tommaso Del Rosso and Karlo Queiroz da Costa

Additional information is available at the end of the chapter

http://dx.doi.org/10.5772/intechopen.70522

Abstract

The influence of a dielectric shell on metallic spherical nanoparticles [core-shell nanoparticles (CSNps)] in the resonant modal response of a surface plasmon resonance (SPR)-type sensor is presented. The planar multilayer sensor structure, based on the Kretschmann and surface plasmon coupled emission (SPCE) configurations, is coupled to a periodic array of these nanoparticles. In the first configuration, the CSNps are considered as a homogeneous layer with effective permittivity given by the Clausius-Mossotti mixing formula and polarizability of a core shell for a quasi-static scattering regime. In the second configuration, it performed an evaluation via the discrete complex image method (DCIM). Electromagnetic wave propagation is evaluated by the generalized reflection coefficient for multilayer structures. The analytical results are validated by numerical simulations performed via finite element method and also by experimental data. We observed that the dielectric shell thickness affects considerably the sensibility of the sensor when analyzing the change in other parameters of the CSNps array.

Keywords: SPR sensor, wave propagation, modal analysis, core-shell metallic nanoparticle, Kretschmann sensor, SPCE configuration

1. Introduction

Surface plasmon resonance (SPR) sensor is a photonic device capable to detect sensitive variations in the effective electromagnetic refraction index near its multi-layered structure,

which can be related to intermolecular interactions or the detection of immobilized analytes, from the interaction between the analyzed samples and the evanescent field generated by surface plasmon polaritons (SPPs) wave, which propagate in the metal-dielectric interface [1].

Despite the first observations of the SPP that have been referenced at the beginning of the last century [2, 3], only at the beginning of the 1980s, SPP-based devices began to be applied to optical sensors with applications in gas detection and biosensors [4, 5], characterizing and quantifying biomolecular interactions [6], medical diagnostics, and viral monitoring [7], among others. The researches in SPR sensors have been increased mainly due to the development of modern nanofabrication techniques, such as the colloidal lithography, focused ion beam (FIB), and electron beam lithography (EBL) [8].

We evaluate an SPR sensor based on Kretschmann configuration (KR) [9] and surface plasmon coupled emission (SPCE) [10] coupled to the periodic array of (CSNps), which can represent the surface immobilization of metal nanopollutants generated, for example, from the nanocomposites manufacturing process [11]. The former has a structure (**Figure 1**) comprising a multilayer formed by a prism (dielectric), a thin metal film (gold), a dielectric spacer (silicon dioxide), the periodic array of CSNps and air. The second one has a similar structure (**Figure 10**) and differs from the first one by the direct incidence of the optical excitation over the immobilized nanoparticles and by the suppression of a layer.

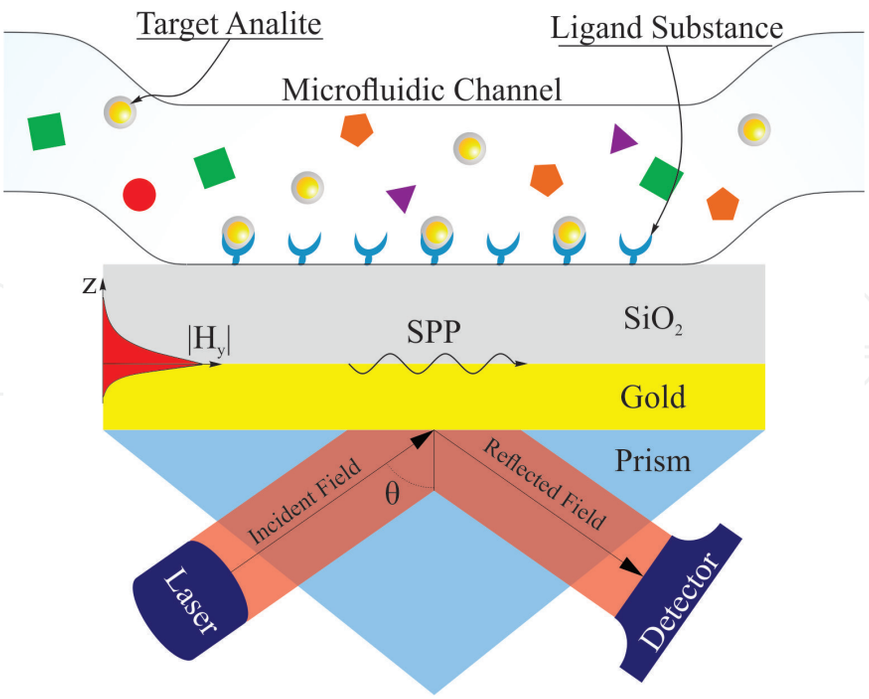

Figure 1. A functional illustration of the SPR sensor based on Kretschmann configuration, coupled to a microfluidic channel with a sample to analyze.

http://dx.doi.org/10.5772/intechopen.70522

2. Kretschmann configuration

2.1. Functioning description

A functional illustration of the SPR sensor based on the Kretschmann configuration is shown in **Figure 1**, where the structure is coupled to a microfluidic channel with a sample flowing at a controlled rate, while a ligand substance immobilizes only the target nanoparticles (analytes) in the functionalized sensor surface. The optical excitation, coupled through the prism, is linearly polarized on transversal magnetic (TM) or transversal electric (TE) and configured in angular modulation, this is with fixed wavelength λ = 632.8 nm and variable incidence angle θ [1]. The intensities of the incident and reflected beams are used to determine the angular reflectivity $\Gamma(\theta)$ curve, which is the base information to determine the sensor response.

For TM polarization, the SPP is excited in the gold-SiO_2 interface (**Figure 1**) when the phase condition $\mathrm{Re}\{\beta\} = k_0\sqrt{\varepsilon_p}\sin(\theta)$ matches only for θ greater than the attenuated total reflection (ATR) angle, which implies in a trough point of $\Gamma(\theta)$ [12]. The parameter β is the SPP complex propagation constant, ε_p is the prism electric permittivity, and k_0 is the propagation constant in free space [13].

The alterations in $\Gamma(\theta)$ can be related to the analytes because the coupling conditions of the SPP wave change when the sample material interacts with the sensor field. In this case, we use the angular shifting ($\Delta\theta$) of the minimum points in $\Gamma(\theta)$ as the sensor output, and thus, the sensor sensibility is proportional to $\Delta\theta$ [1].

The extra dielectric layer allows the excitation of multiple resonant wave modes, like guides modes, even in TE polarization [12]. Using both TE and TM $\Gamma(\theta)$ curves, the amount of information about the CSNps increases and improves the estimation of parameters such as surface density, size, and distance between immobilized nanopollutants [1, 14]. This parametric estimation can be performed using the approximated model of Clausius-Mossotti, or even using tools such as Winspal free software [15].

2.2. Theoretical modeling

The SPR sensor in **Figure 1** is modeled by the multilayer planar structure depicted in **Figure 2**. The incident beam, reflected beam, and incidence angle θ refer internally to the prism. The CSNps have a dielectric shell of thickness b, composed of fused silica for this study, to provide stability to a nanoparticle, preventing agglomeration, and decreasing their surface interaction [16]. The periodic planar array of CSNps is described by the geometric period of $d + 2(a + b)$, where a is the nanoparticle core radius and d is the distance between them.

The applied relative permittivity was prism (SF4) ε_p = 3.0615, gold film ε_{Au} = − 11.66 + 1.35i[1], and SiO_2 ε_d = 2.132 [15, 17]. The CSNps array is treated as a homogeneous layer with thickness of $h_{CS} = 2(a + b)$ and effective permittivity ε_{eff} in Eq. (1), given by the Clausius-Mossotti

[1]Obtained from the Lorentz-Drude model with one term of interband and time dependence with $\exp(-i\omega t)$.

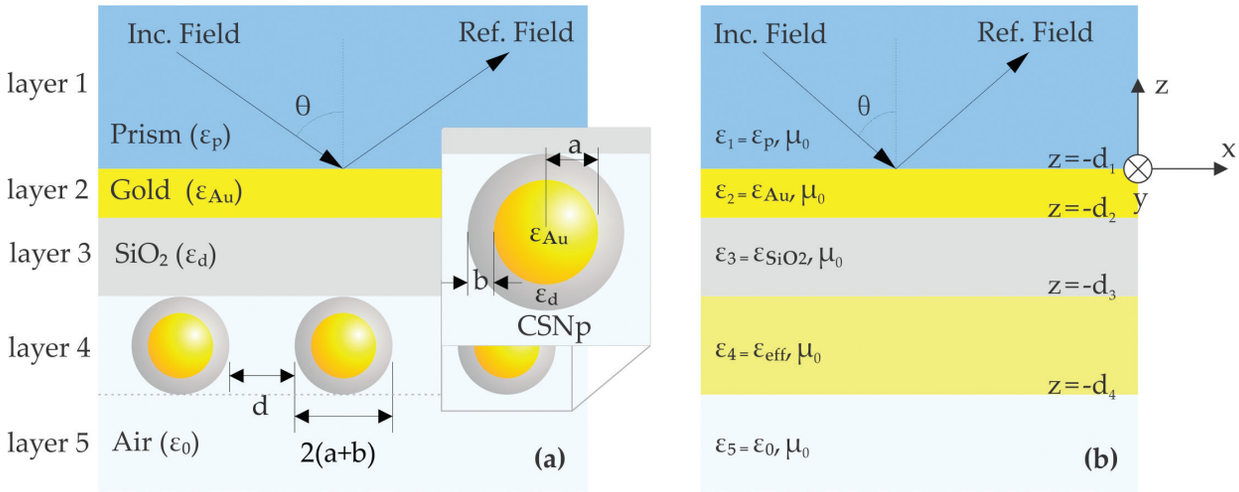

Figure 2. (a) The multilayer structure model of the SPR sensor coupled to the periodic array of CSNps. The inset highlights the CSNps with gold-core (ε_{Au}) of radius a and dielectric shell (ε_d) of thickness b; (b) Resulting planar structure using the effective layer to approximate the CSNps array.

mixing formula and the core-shell polarizability of [18], set to the quasi-static scattering regime [13, 19]. The resulting planar structure of the sensor is shown in **Figure 2(b)**.

$$\varepsilon_{eff} = \varepsilon_0 \left(\frac{1 - 2f_s \Lambda}{1 - f_s \Lambda} \right) \tag{1}$$

In Eq. (1): $f_s = 2\pi/3[(a+b)/(d+2(a+b))]^2$is the CSNps volume fraction in the planar array; and the parameter Λ is defined in Eq. (2), where $f = a^3/(a+b)^3$ is the core volume fraction in the CSNps [19]. The parameter f_s is zero for no immobilized CSNps ($\varepsilon_{eff} = \varepsilon_0$) and $f_s = \pi/6 \simeq 52.36\%$ when the distance d is zero. To eliminate the shell of the CSNps, we set $\varepsilon_d = \varepsilon_0$ and $b = 0$ nm in Eq. (2), obtaining the Maxwell-Garnett mixing formula [20, 21]

$$\Lambda = \frac{f(\varepsilon_{Au} - \varepsilon_d)(\varepsilon_0 + 2\varepsilon_d) + (\varepsilon_{Au} + 2\varepsilon_d)(\varepsilon_d - \varepsilon_0)}{f(\varepsilon_{Au} - \varepsilon_d)(2\varepsilon_d - \varepsilon_0) + (\varepsilon_{Au} + 2\varepsilon_d)(2\varepsilon_d + \varepsilon_0)} \tag{2}$$

The propagation of the electromagnetic wave in the sensor planar structure (**Figure 1(b)**) is performed, in the frequency domain with time dependence of $\exp(-i\omega t)$, by the generalized reflection coefficient in Eq. (3), which considers the multiple reflections and transmissions in all layers [22]. In Eqs. (3) and (5), $R_{n,n+1}$ and $T_{n,n+1}$ are the Fresnel's reflection and transmission coefficients, respectively, set to TM or TE polarization in accordance with the excitation. For TM case, the transverse magnetic field $H_{n,y}$ in the n-th layer is given in Eq. (4) and for TE case, Eq. (4) is set to the electric field $E_{n,y}$. In Eq. (4), A_n is the field amplitude in the n-th layer, given by Eq. (5).

$$\tilde{R}_{n,n+1} = \frac{R_{n,n+1} + \tilde{R}_{n+1,n+2} \exp\left[i2k_{n,z}(d_{n+1} - d_n)\right]}{1 + R_{n,n+1}\tilde{R}_{n+1,n+2} \exp\left[i2k_{n,z}(d_{n+1} - d_n)\right]} \tag{3}$$

$$H_{n,y} = A_n \left[\exp\left(-ik_{n,z} z\right) + \tilde{R}_{n,n+1} \exp\left(ik_{n,z}\left(z + 2d_n\right)\right) \right] \exp\left(ik_x x\right) \tag{4}$$

http://dx.doi.org/10.5772/intechopen.70522

$$A_n = \frac{T_{n-1,n} A_{n-1} \exp\left[i(k_{n-1,z} - k_{n,z}) d_{n-1}\right]}{1 - R_{n,n-1} \tilde{R}_{n,n+1} \exp\left[i2k_{n+1,z}(d_{n+1} - d_n)\right]} \tag{5}$$

For the recursive expressions, Eqs. (3)–(5): $A_1 = 1$ is the incident field amplitude in prism layer; $k_n^2 = k_0^2 \varepsilon_n$ is the propagation constant in the n-th layer, considering no magnetics in all the materials; $k_x = k_1 \sin(\theta)$ is the wave vector in x-axis direction, which is the same for all layers; and $\tilde{R}_{N,N+1} = 0$ is the reflection coefficient in the last layer, where $N = 5$ is the number of layers in the sensor structure (**Figure 2(b)**) [22]. The angular reflectivity curve is obtained from Eq. (3) for the gold-SiO_2 interface by $\Gamma(\theta) = \left|\tilde{R}_{1,2}\right|^2$.

2.3. Model validation and modal analysis

Herein, we compare the approximate analytical model with the results obtained by numerical simulations and experimental data to achieve the theoretical consistency between the models and study the parametric interval for validation. The numerical results were obtained through the 3D simulation environment COMSOL Multiphysics, based on the finite element method [23]. We obtained the experimental data from the SPR spectrometer described in [24], which uses a He-Ne laser as the excitation source and a rotary base to control the incident angle. The sensor's structure is fabricated by e-beam vacuum deposition process.

In **Figure 3**, we compare the analytical (An.), numerical (Num.), and experimental (Exp.) $\Gamma(\theta)$ curves for no CSNps case. The experimental curves are restricted in θ to the interval of TM2 and TM1 modes in **Figure 3(a)** due to limitations in the SPR spectrometer [15, 24]. The thickness of the sensor structure used in **Figure 3** was estimated by curve fitting using the free software Winspal [15]. The minimum of $\Gamma(\theta)$ highlights in **Figure 3** represents the resonant guide modes of order 1 (TM1 and TE1), order 2 (TM2 and TE2), and the SPP[2] mode [12].

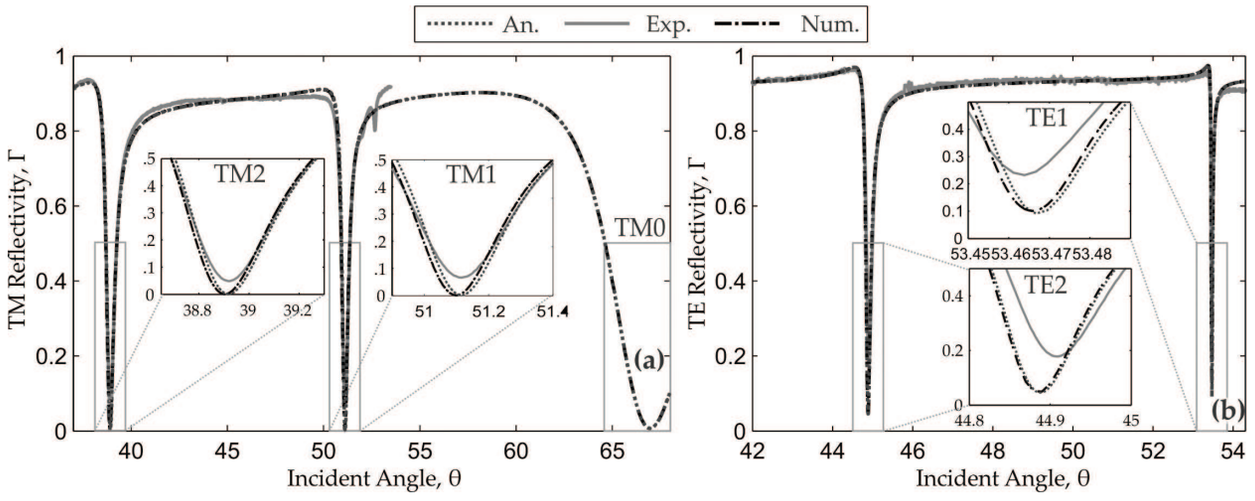

Figure 3. Comparison of the angular reflectivity curves Exp., An., and Num. for no CSNps on the sensor for (a) TM polarization and (b) TE polarization. The layer's thickness in the structure is t_{Au} = 48 nm and t_{SiO_2} = 677 nm.

[2]The SPP wave is named TM0, this is a zero-order guide mode in TM polarization.

The deviations An.-Exp. and Num.-Exp. in **Figure 3** are 2.39 and 2.12% for the TM curves, and 1.97 and 2.05% for the TE curves, showing high accuracy for the numerical simulation and the analytical model. The differences may be due to measurement errors and roughness in the fabricated multilayer structure [15, 24].

Figure 4 shows the magnitudes of the transversal fields, in the *z*-axis of **Figure 2(b)**, for the resonant mode highlights in **Figure 3**. One can note in **Figure 4(a)** the high field amplitude in the gold-SiO_2 interface for the TM0 mode and its characteristic evanescent field in both gold and SiO_2 layers [13]. This is also observed for the modes TM1 (**Figure 4(b)**) and TM2 (**Figure 4(c)**), but with a predominant intensity in the SiO_2 layer, like guide modes [12]. For the TE modes TE1 (**Figure 4(d)**) and TE2 (**Figure 4(e)**), there is no surface wave in the gold-SiO_2 interface because the plasmonic wave only exists for TM polarization [13].

To validate the analytical model, in **Figure 5**, we compare it with Num. simulations in three cases for the sensor: (i) No CSNps; (ii) CSNps with $b = 0$ nm; and (iii) CSNps with $b = 10$ nm. The relative deviation An.-Num. in **Figure 5** are 8.88% ($b = 0$ nm) and 9.18% ($b = 10$ nm) for the TM curves, and 0.74% ($b = 0$ nm) and 1.22% ($b = 10$ nm) for the TE curves. Therefore, the deviation An.-Num. tends to increase for tested values of b, and a possible cause is the increase of the CSNps size.

The hypothesis that generally increases the relative deviation characterizes the An. model limitation, such as (A) scattering losses [13, 21]; (B) dipole field interaction between CSNps in the array [18]; and (C) the restriction as thin of the effective layer thickness [12, 19]. As (A) grows with the CSNp size (parameters a and b), the relative deviation tends to increase with a and b, so, these parameters need to be restricted [19]. The phenomenon (B) and the relative deviation decrease with the distance d in the array, because this here is used the minimum

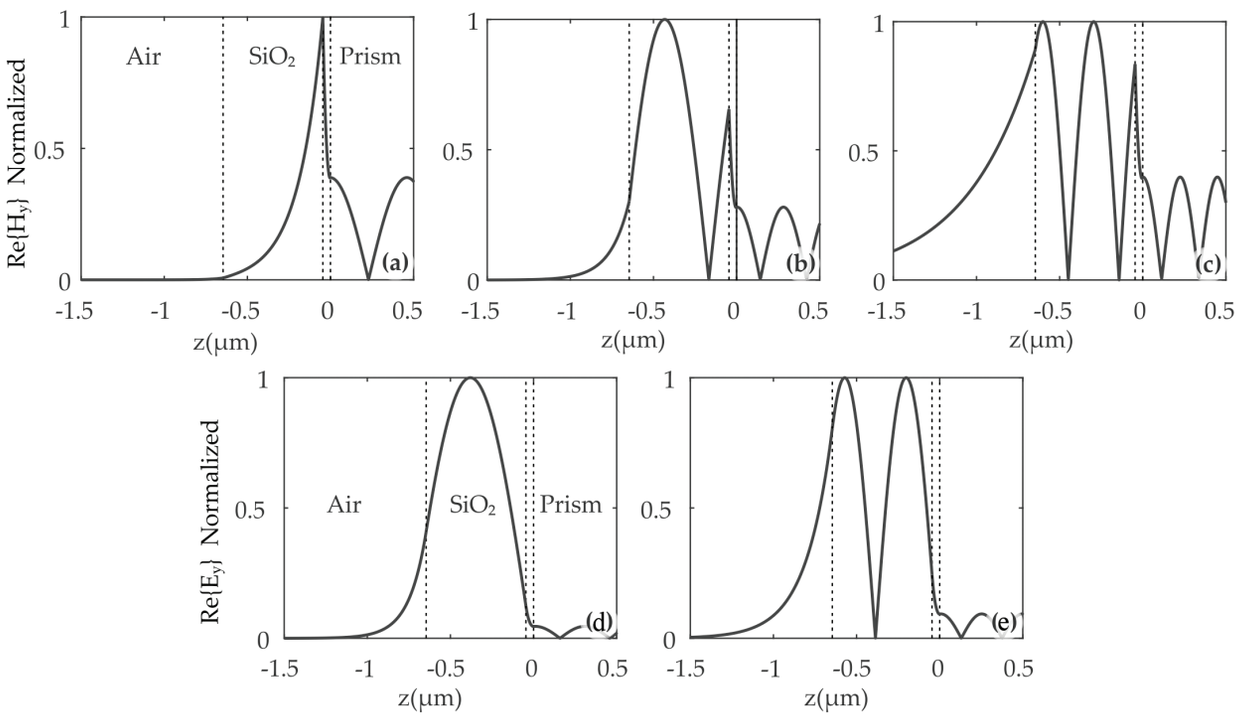

Figure 4. Magnitude of the transversal field in *z*-axis of **Figure 2(b)** for the resonant modes highlights in **Figure 3(a)**: (a) TM0 in $\theta = 67°$, (b) TM1 in $\theta = 51.11°$, (c) TM2 in $\theta = 38.92°$; and in **Figure 3(b)**: (d) TE1 in $\theta = 53.465°$, (e) TE2 in $\theta = 44.88°$.

http://dx.doi.org/10.5772/intechopen.70522

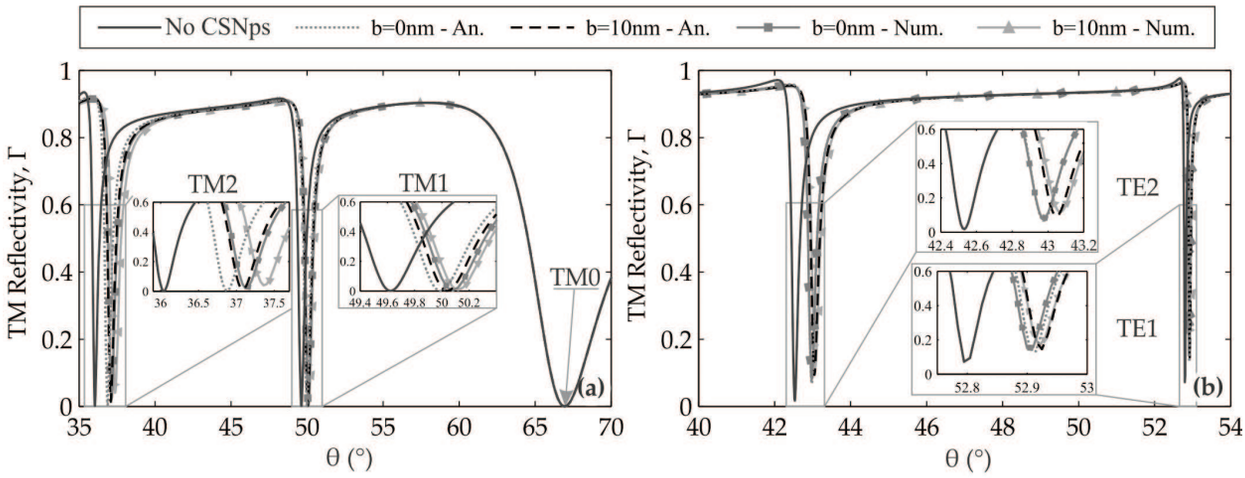

Figure 5. Comparison of the An. and Num. curves for the cases (i) No CSNps; (ii) CSNps with fixe b = 0 nm; and (iii) CSNps with fixe b = 10 nm. (a) TM polarization and (b) TE polarization. For all cases are set the fixed parameters a = 30 nm, d = 100 nm, t_{Au} = 46 nm, and t_{SiO_2} = 600 nm.

value of d = 50 nm. The limitation (C) can modify the direct and inverse behavior in the relative deviation with the limitations (A) and (B), respectively, for other values of a and d.

In **Figure 6**, we compare the An. and Num. real magnetic fields, in the zx-plane of **Figure 2(b)**, for the mode minimum points in the TM curve b = 10 nm of **Figure 5(a)**. Note that, in general, the An. and Num. results are very similar, differing basically due to the high field amplitude in the metal-core surface of the nanoparticles (**Figure 6(b)**, **(d)**).

Based on **Figure 6**, in **Figure 7**, we compare the An. and Num. transversal fields for the TE curve b = 10 nm of **Figure 5(b)**. Different from the TM fields in **Figure 6**, the TE mode fields present a low field amplitude in the shell and a constant electric field in the CSNps metal core. The visual analysis of **Figures 4–7** indicates a greater interaction with the sensing layer for the wave modes in which the minimum region is closest to the ATR angle, even for TE modes,

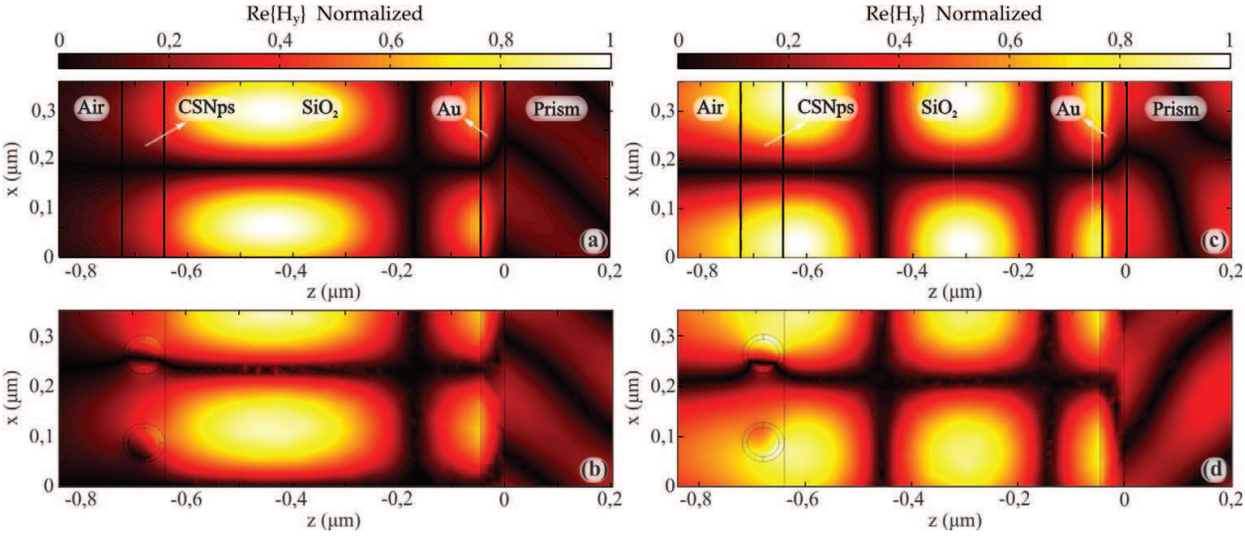

Figure 6. Comparison of the An. and Num. real magnetic fields for the TM modes in **Figure 5(a)**, for the curve b = 10 nm. An.: (a) TM1 in θ = 50.04° and (c) TM2 in θ = 37.09°; and Num.: (b) TM1 in θ = 50.12°; and (d) TM2 in θ = 37.36°.

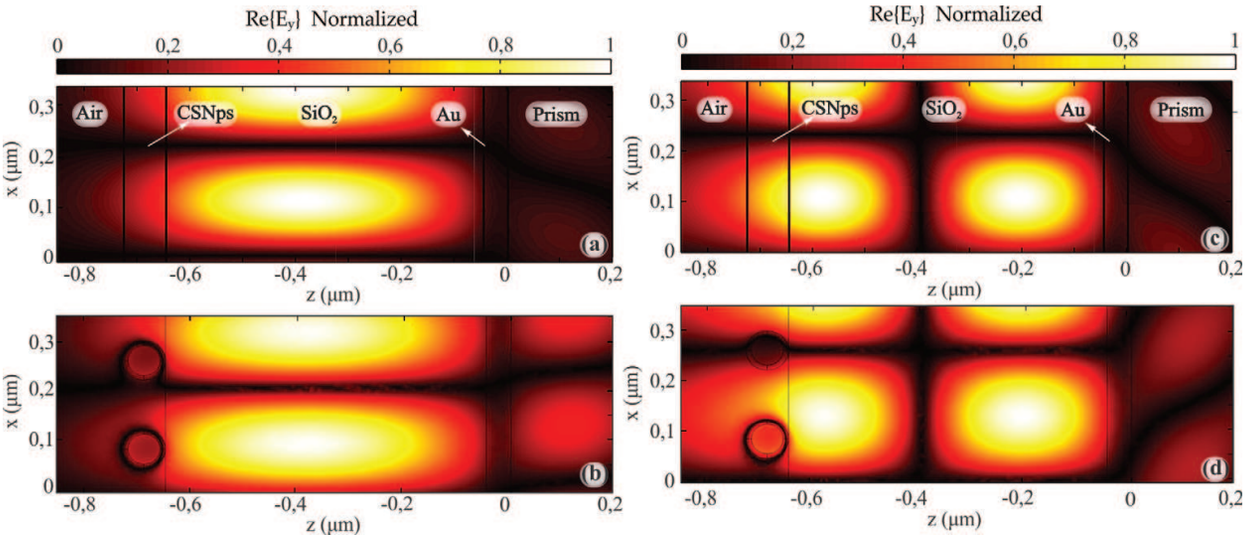

Figure 7. Comparison of the An. and Num. real electric fields for the TE modes in **Figure 5(b)**, curve $b = 10$ nm. An.: (a) TE1 in $\theta = 52.93°$ and (c) TE2 in $\theta = 43.04°$; Num.: (b) TE1 in $\theta = 52.92°$ and (d) TE2 in $\theta = 43.07°$.

because of the greater field intensity and the consequent greater interaction with the CSNps [25]. In [17], one can note that the thickness of the SiO_2 layer, in the sensor structure, can regulate the reflectivity minimum point of the resonant wave modes, and the wave order in the same curve, so this parameter can improve the sensor sensibility.

2.4. Sensitivity analysis

To evaluate the sensibility, we vary the CSNps array parameters a, b, and d, and calculate the angular shift $\Delta\theta$ only for the more sensitive TM2 mode in the minimum points of $\Gamma(\theta)$. First,

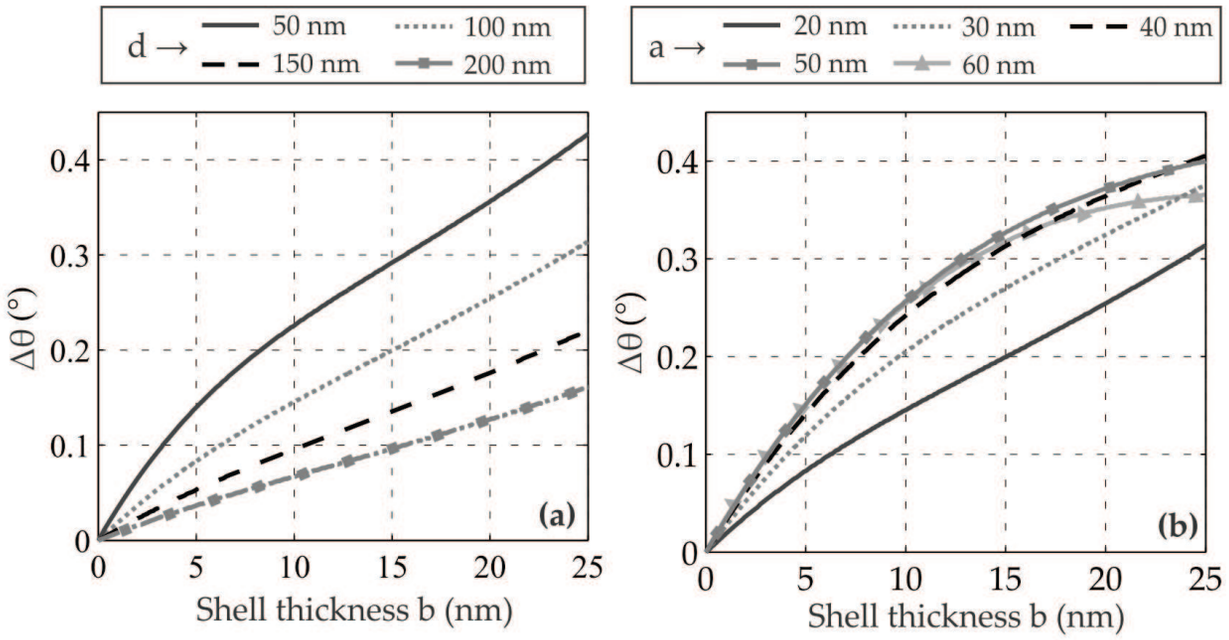

Figure 8. Curves of $\Delta\theta \times b$ for the values of: (a) distance $d = 50$, 100, 150, and 200 nm, and the fixed parameter $a = 20$ nm; and (b) radius $a = 20$, 30, 40, 50, and 60 nm, and the fixed $d = 100$ nm.

we analyze the sensibility to one of the parameters, and then we verify how other parameters influence in the sensibility, setting some different values. For this analysis, we use only the analytical model, that presents low costs in computing, and the fixed parameters were t_{Au} = 46 nm and t_{SiO_2} = 600 nm.

2.4.1. Sensitivity to the shell thickness b

In **Figure 8**, we present the curves of $\Delta\theta$ in function of b ($\Delta\theta \times b$ curve), relative to the initial curve b = 0 nm. In **Figure 8(a)**, each curve is defined for different values of the distance d and in **Figure 8(b)**, they are for values of a. The shifting of the minimum region to right is the positive direction of the $\Delta\theta$.

Note in **Figure 8(a)**, $\Delta\theta \times b$ decreases as d increases, which declines the sensor sensibility. However, higher values of d decrease, in general, the sensor sensitivity and the contrary are true for lower values of d. For the parameter a, the sensitivity by the curves $\Delta\theta \times b$ in **Figure 8(b)** increases for the most cases, but for the curves a = 50 nm and a = 60 nm, one can visualize the tendency of an inverse behavior. This can turn the CSNps characterizing process more complex because we can obtain, for the same value of $\Delta\theta$, more than one value of b. To avoid this, we can restrict a < 50 nm and b < 20 nm.

2.4.2. Sensitivity to the distance d

Figure 9 presents the $\Delta\theta$ of TM2 mode in function of d ($\Delta\theta \times d$ curve), relative to the initial curve d = 50 nm. In **Figure 9(a)**, the curves differ in the values of b and in **Figure 9(b)** in the values of a. The increasing of d, corresponding to the concentration decrease of the immobilized CSNps on the sensor, basically, its shifts the minimum points to left, explaining the negative

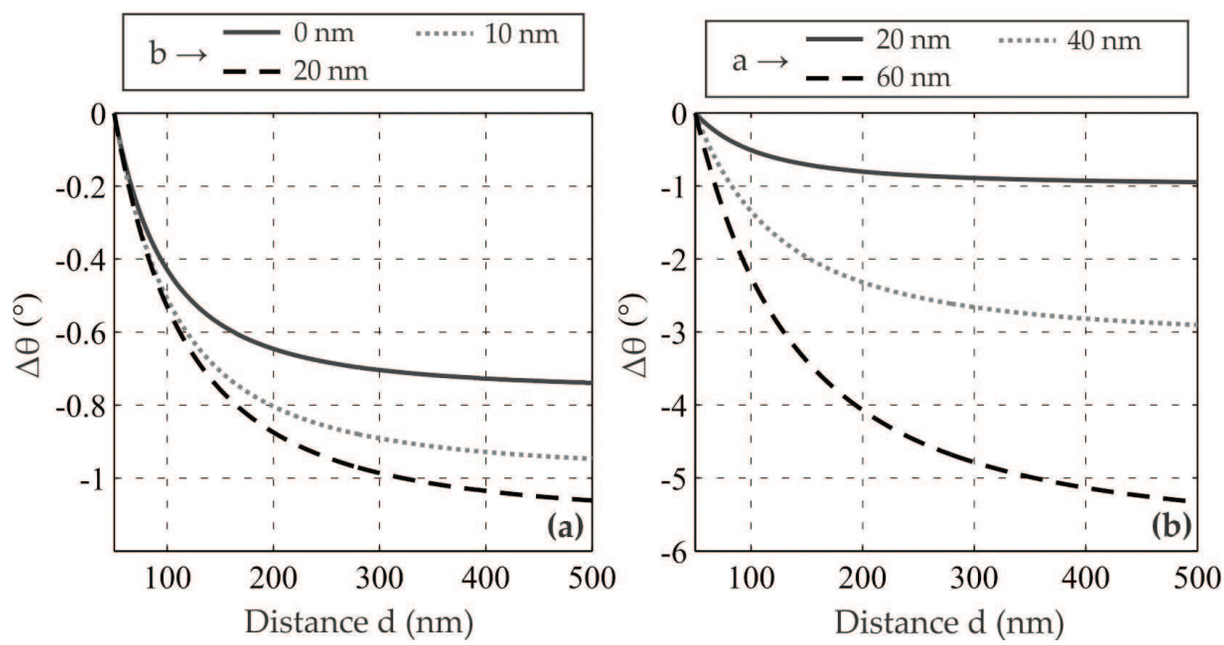

Figure 9. Curves of $\Delta\theta \times d$ for TM2 modes for the values of: (a) dielectric shell thickness b = 0, 10, and 20 nm, and the fixed parameter a = 20 nm; and (b) radius core a = 20, 40, and 60 nm, and the fixed parameter b = 10 nm.

values of $\Delta\theta$ in **Figure 9**. In **Figure 9**, the great sensitivity response when CSNps are quite close or for small values of d.

In **Figure 9(a)** we note that the increasing of b results in greater values of $\Delta\theta$, this is a better sensitivity response of the sensor. In **Figure 9(b)**, we can observe that both parameters a and b increase the sensor response because the sensor is more sensitive to variation in the CSNps core radius. This behavior was also observed in [17] and is expected due to the increase of the resonant field interaction with the array when the metal core of the CSNps is bigger. While b increases, it increases the CSNps size, decreasing the field interaction.

3. SPCE configuration

3.1. Functional description

The functioning of an SPR sensor in SPCE configuration (**Figure 10**) is based on the interaction of the field radiated by the immobilized analytes with the sensor structure, composed by a thin metal film deposited on the prism [10]. These interactions generate the SPP wave on the air-gold surface and radiating modes in the prism, that is a high directional emission in a specific SPCE angle and depending on the nanoparticle [26]. The high directional nature of the SPCE emission also increases the efficiency of coupled emission detection [27]. Similar to the sensor in the Kretschmann configuration, here the SPCE configuration is excited by a laser beam operating at the wavelength of 632.8 nm.

In **Figure 10(a)**, the sensor in the SPCE configuration is illustrated. First, a solution with the suspended analytes flows in the microfluidic channel while the target nanoparticles are immobilized on the sensor surface by a specific ligand substance. Then, the solution flow is cut off and drained until only the immobilized CSNps remain to be analyzed. The CSNps

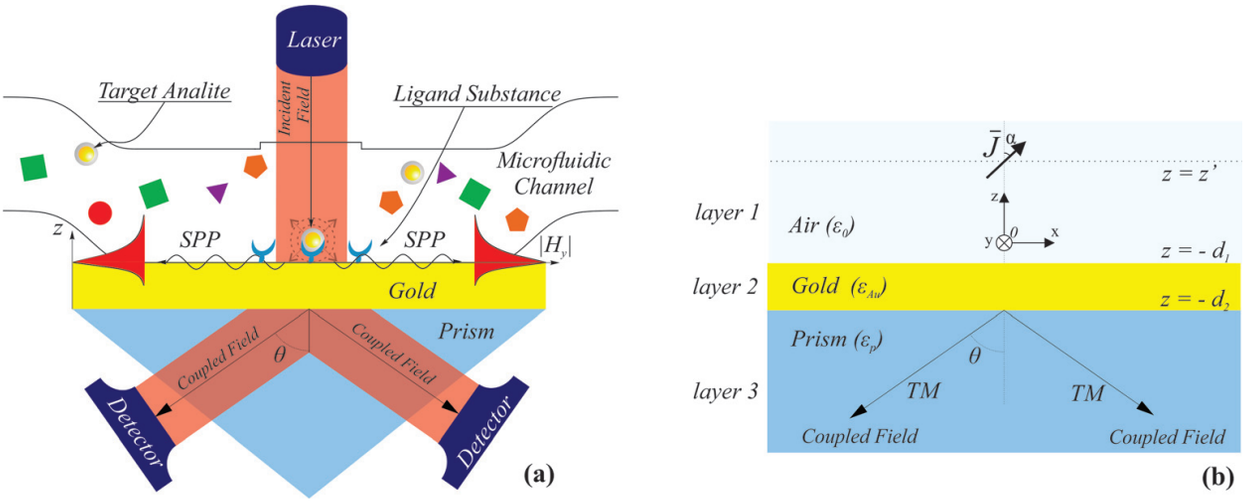

Figure 10. (a) A functional illustration of the analyzed SPCE sensor coupled to a microfluidic channel. (b) The approximate model of the SPCE sensor in (a) by a multilayered planar structure and a resonant dipole.

can be held by the ligand substance at z' or by a dielectric spacer of same thickness with a ligand substance of negligible height. An optical detector evaluates the SPCE angle of the analyte [28].

An approximate model of the sensor in **Figure 10(a)** is presented in **Figure 10(b)**, where the structure is a planar multilayer with three layers: air, thin gold film, and SF4 optical prism, all represented by their respective complex permittivity. The interaction of the laser beam with the analytes and their re-annealing is equivalently modeled by a dipole, which represents the immobilized CSNps and is situated at the height z' in the layer 1 of **Figure 10(b)**.

Although the dipole-type optical emitter is nonpolarized, the coupled field targeting the detector in **Figure 10(b)** is highly polarized in the TM [29]. This occurs because part of the CSNps emission is naturally in the TM polarization and can excite the SPP wave on the air-gold interface, which evanescent wave passes through the thin metallic layer and radiate in the prism as a propagating wave polarized in the TM polarization. Therefore, the SPR sensor in the SPCE configuration can be understood as a reverse functioning of the Kretschmann configuration.

Note the existence of different nanoparticles in the fluidic channel (**Figure 10(a)**); however, only the target nanoparticles are immobilized on the sensor surface. Here, the sensor is analyzed with only immobilized CSNps and the result is a radiating TM field in a specific angle of coupling in the prism that corresponds to this nanoparticle. However, when using different ligand substances, for multichannel evaluation, different coupling angles would be detected, each angle related to a different particle of interest [30].

3.2. Theoretical modeling

For the SPR sensor in SPCE configuration, the SPP wave is created from interactions of the sensor structure and immobilized nanoparticles, which emit radiation and evanescent field when excited by a source. In the SPCE sensor, the nanoparticles on the substrate have dimensions smaller than the excitation wavelength, so they are represented here by infinitesimal dipoles with equivalent dipole moments or by elementary currents given by Eq. (6) [31, 32]:

$$\bar{\mathrm{J}} = \bar{\mathrm{J}}_{0p}\delta(\bar{r},\bar{r}_p) = \left(\xi_p \overline{E}_p^t\right)\delta(\bar{r},\bar{r}_p) = \xi_p\left[\overline{E}_i(\bar{r}_p) + \overline{E}_r(\bar{r}_p) + \sum_{q=1,\, q\neq p}^{N} \overline{E}_{dip}^q(\bar{r}_p) + \sum_{q=1}^{N} \overline{E}_r^q(\bar{r}_p)\right]\delta(\bar{r},\bar{r}_p) \quad (6)$$

The elementary current of the equivalent dipole is orientated by the laser source. To determine the induced dipole moments of an array of P dipoles on a multilayer structure, one must solve the following system of linear equations for p, $q \in \{1,2, \ldots, P\}$, where $\bar{r}_p$ are the positions of the P dipoles, $\overline{E}_p^t$ is the total external field of excitation on the equivalent dipole, that is the sum of all the fields that arrive in the dipole p, and ξ_p is the polarization constant that depends on the type of element considered (CSNps, biomolecules, QDs) [31].

For the total $\overline{E}_p^t$ in Eq. (6), that has four terms, is considered a linear dependence with the dipole. The first term of $\overline{E}_p^t$ represents the incident field, the second one, the reflection of the field incident on the structure, the third term, the radiation of each dipole, and the fourth term, the reflections in the structure of the field radiated by each dipole.

The total electric field of the dipole defined in Eq. (6), for an arbitrary direction in a homogeneous medium, can be derived from the dyadic Green's functions in Eq. (7) [32]:

$$\widehat{G}^e\left(\overline{r},\overline{r}'\right) = i\omega\mu\left(\widehat{I} + \frac{1}{k^2}\nabla\nabla\right)\bar{\mathrm{J}}\frac{e^{jk\left|\overline{r}-\overline{r}'\right|}}{4\pi\left|\overline{r}-\overline{r}'\right|} \tag{7}$$

where $\widehat{I}$ is a unitary dyad, $\overline{r}$ is the point of observation, and $\overline{r}'$ is the source point. The dipoles irradiated nonpolarized spherical waves; thus, a spherical wave radiated can be expanded as an integral of conical or cylindrical waves in the direction ρ times a plane wave in the z-direction, over all propagation constant $k_\rho = \sqrt{k - k_z}$. It is possible to relate spherical waves with plane waves from the integral Sommerfeld identity in Eq. (8) [33]:

$$\frac{\exp\left(ik\left|\overline{r}-\overline{r}'\right|\right)}{\left|\overline{r}-\overline{r}'\right|} = \frac{i}{2}\int_{-\infty}^{+\infty} dk_\rho k_\rho H_0^2\left(k_\rho\rho\right)\frac{\exp\left(ik_z\left|z-z'\right|\right)}{k_z} \tag{8}$$

The identity in Eq. (8) can be obtained from the solution of the scalar wave equation, obtained first in spherical coordinates, and later in rectangular coordinates using the three-dimensional Fourier transform. For simplicity, only the z-direction component is evaluated, thus, the formalism of a vertical dipole VED is possible to be used. Substituting Eq. (8) in Eq. (7), it can be shown that the field $E_{n,z}$ in an n multiple-layered structure in the presence of a resonant dipole can be represented by Eq. (9) [22]:

$$E_{n,z} = -\frac{\mathrm{J}_z}{4\pi\omega\varepsilon_n}\int_{-\infty}^{+\infty} dk_\rho \frac{k_\rho^3}{2k_{1z}} H_0^2\left(k_\rho\rho\right) A_n^{TM}\left[\exp\left(ik_{n,z}|z|\right) + \tilde{R}_{n,n+1}^{TM}\exp\left(ik_{n,z}(z+2d_n)\right)\right]\exp\left(ik_{1z}z'\right) \tag{9}$$

where A_n^{TM} and $\tilde{R}_{n,n+1}^{TM}$ are the same parameters defined in Eqs. (5) and (3), respectively, over all propagation constantk_ρ. Eq. (9) is here rewritten in terms of the zero-order Bessel function in Eq. (10):

$$E_{n,z} = \frac{i\mathrm{J}_z}{4\pi\omega\varepsilon_n}\left[\int_0^{+\infty} dk_\rho k_\rho J_0\left(k_\rho\rho\right)\frac{\tilde{f}_{n,z}^s\left(k_z,z,z'\right)e^{ik_{n,z}\left|z-z'\right|}}{k_{n,z}} + \int_0^{+\infty} dk_\rho k_\rho J_0\left(k_\rho\rho\right)\frac{\tilde{f}_{n,z}^r\left(k_z,z,z'\right)e^{ik_{n,z}\left|z-z'\right|}}{k_{n,z}}\right] \tag{10}$$

where $\tilde{f}_{n,z}^s\left(k_z,z,z'\right)$ and $\tilde{f}_{n,z}^r\left(k_z,z,z'\right)$ are the spectral functions defined in Eqs. (11) and (12), respectively:

http://dx.doi.org/10.5772/intechopen.70522

$$\tilde{f}^{s}_{n,z}\left(k_z, z, z^{'}\right) = \frac{ik_{n,z}k_{\rho}^{2}A_{n}^{TM}\exp\left[-i\left(k_{n,z}z - k_{1z}z^{'}\right)\right]}{k_{1z}\exp\left(ik_{n,z}|z - z^{'}|\right)} \tag{11}$$

$$\frac{\tilde{f}^{r}_{n,z}(k_z, z, z') = ik_{n,z}k_{\rho}^{2}A_{n}^{TM}\tilde{R}^{TM}_{n,n+1}\exp\left[i(k_{n,z}(z + 2d_n) + k_{1z}z')\right]}{k_{1z}\exp\left(ik_{n,z}|z - z'|\right)} \tag{12}$$

where indices *s* and *r* are treated here as a spectral contribution related to incidence and reflection in the multilayer structure. These integrals are extremely complicated to calculate and the solutions do not have closed forms. Some difficulties of the integral representation are highlighted [34, 35]: Low integration kernel convergence, branching points, and branch cuts arise, the appearance of functions of double or multiple values, the choice of a single appropriate Riemann surface, possibility of complex poles, among others. That way, the lack of analytical expressions in a closed form combined with a heavy computational cost associated with the direct integration for this integral, which have low convergence, make direct numerical evaluation an impractical approach to our analysis.

When solving problems involving integrals like Eq. (10), several recent approaches have been proposed [36, 37], all consist of the evaluation of spectral functions using the Sommerfeld Identity with variants of the discrete complex image method (DCIM) as an acceleration tool. Here, we evaluate the integral equations directly from the electric field into a versatile application for the use of DCIM and applies the DCIM directly on the integral field equations.

The DCIM method expands the integral equations of (11) and (12) into a sum of complex terms, that is, it estimates values of complex integrals over an integration path in the complex domain, usually with a range of (0, ∞), by a finite number of samples of the integrand. A solution based on a two-level path is used [38]. We use a sophisticated scheme, where the integrand is approximated by a superposition of complex exponentials, and this approximation is semi-analytical since it is not an exact but approximate solution.

3.3. Modal analysis

In this section, we analyze the SPR sensor of **Figure 10(b)** using the same relative permittivity presented in Section 2.2 for the excitation source wavelength of λ = 632.8 nm. It is considered that the radiation of the analyte occurs at this same wavelength. The results are presented for the near and far field.

3.3.1. Numerical example

Figure 11(a) shows the real part of the field E_z in the multilayer structure of **Figure 10(b)** and one can observe that the waves radiated by the immobilized nanoparticles induce the surface plasmonic mode in the air-gold interface, whereas in the prism, formed waves are concentrated at specific angles. **Figure 11(b)** shows that the plasmonic mode is excited throughout the air-gold interface as a cylindrical wave symmetrical to the *z*-axis; it is possible to visualize the excited SPPs on the first interface and the rapid fading of the electric field from the source.

Figure 12(a) shows the two-dimensional radiation diagram of the SPCE sensor, where maintaining the operating wavelength at λ = 632.8 nm makes an evaluation of the intensity of the distant field at different heights: z' = 20, 50, 100, 150, and 200 nm. It is observed that the far

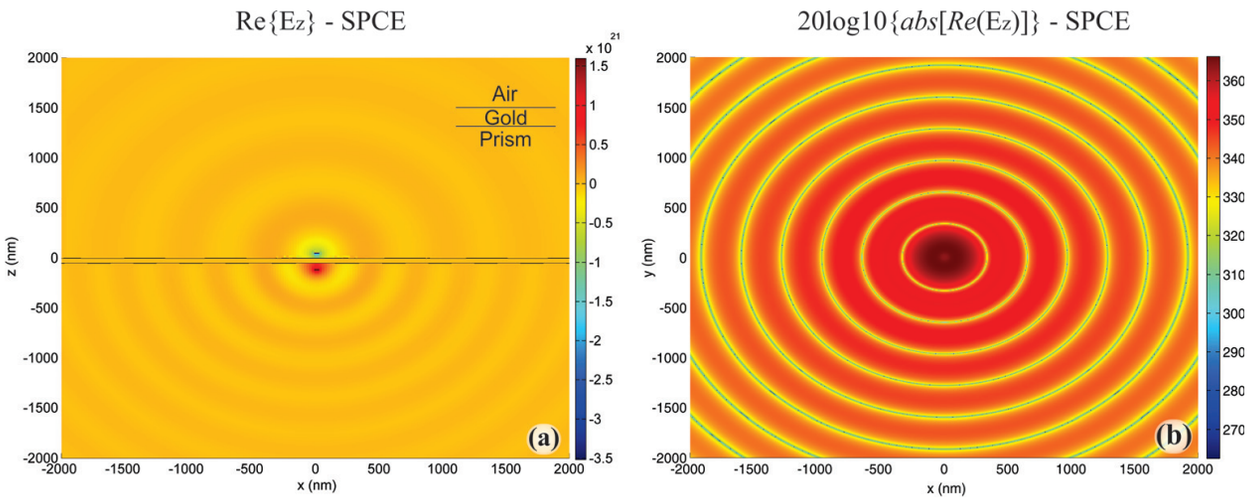

Figure 11. (a) Electric field distribution Re{E_z} obtained via DCIM in all three layers air, gold, and prism (SF4). (b) Electric field distribution 20log10{*abs*[Re(E_z)]} obtained in the *xy* plane via DCIM at the air-gold interface.

field strength is greater for height z' = 20 nm. Note that the intensity of the lower lobes, which depend on the field coupled in the prism, as well as on the upper lobes that depend on the total field in the first layer, increase in intensity according to the decrease in height z'.

Figure 12(b) shows the far field three-dimensional diagram of the SPCE sensor for the permissiveness values presented above and optimized height for z' = 20 nm. The emission coupled to the prism forms a circular cone. Note that the lower lobes have well-directed beams at a very characteristic coupling angle θ = 145.2°, that is, electric field coupled at the angle of θ_{SPCE} = 34.8°.

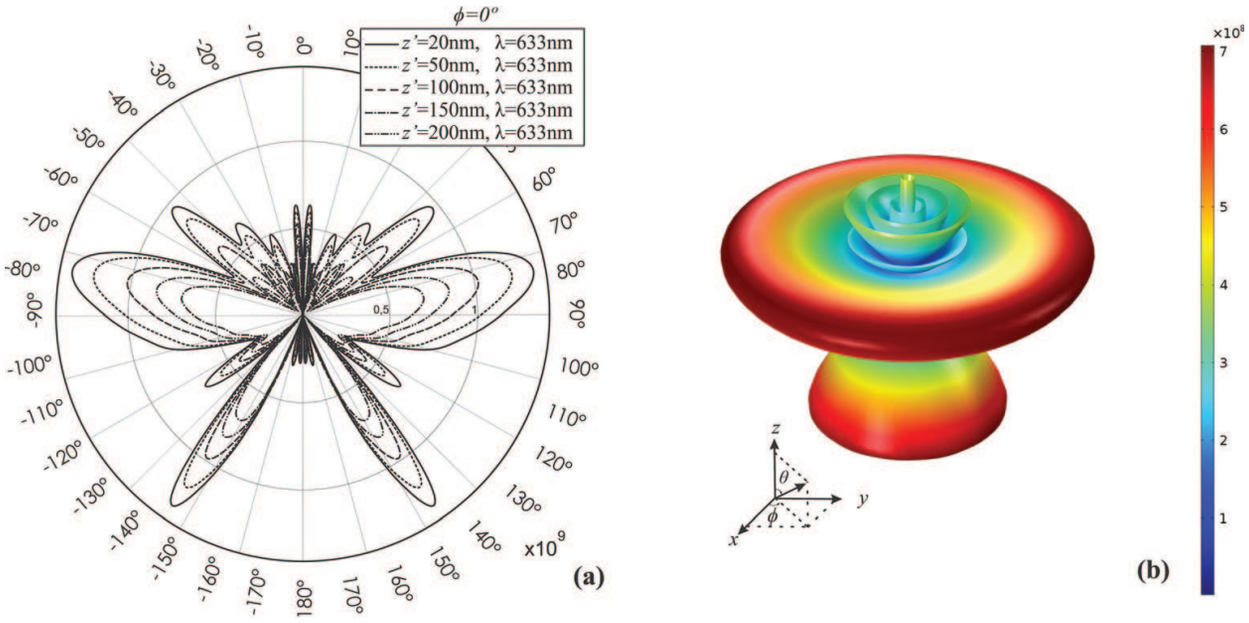

Figure 12. (a) Two-dimensional radiation diagram of the SPCE sensor, evaluation of the intensity of the distant field at different heights: z' = 20, 50, 100, 150, and 200 nm. (b) Far field three-dimensional diagram of the SPCE sensor for optimized height for z' = 20 nm. Note that electric field coupled at the angle of θ_{SPCE} = 34.8°.

http://dx.doi.org/10.5772/intechopen.70522

3.4. Reciprocity between SPR sensors in the KR and SPCE configuration

The SPCE sensor is physically the reverse structure of the KR sensor. In this topic, a previous evaluation of the electromagnetic reciprocity between the KR and SPCE configuration sensors is presented. In both configurations, the same materials are used, that is, air, gold, and prism (SF4). The sensor operates on a standard $\lambda = 632.8$ nm wavelength, with a gold layer of 50 nm thickness.

Figure 13 presents results for evaluation of reciprocity between the KR and SPCE sensors with the configurations described above, where **Figure 13(a)** shows the real part of the *Hy* field for a plane wave over the plasma resonance angle $\theta_{SPP} = 36.8°$ in the KR sensor. **Figure 13(b)**

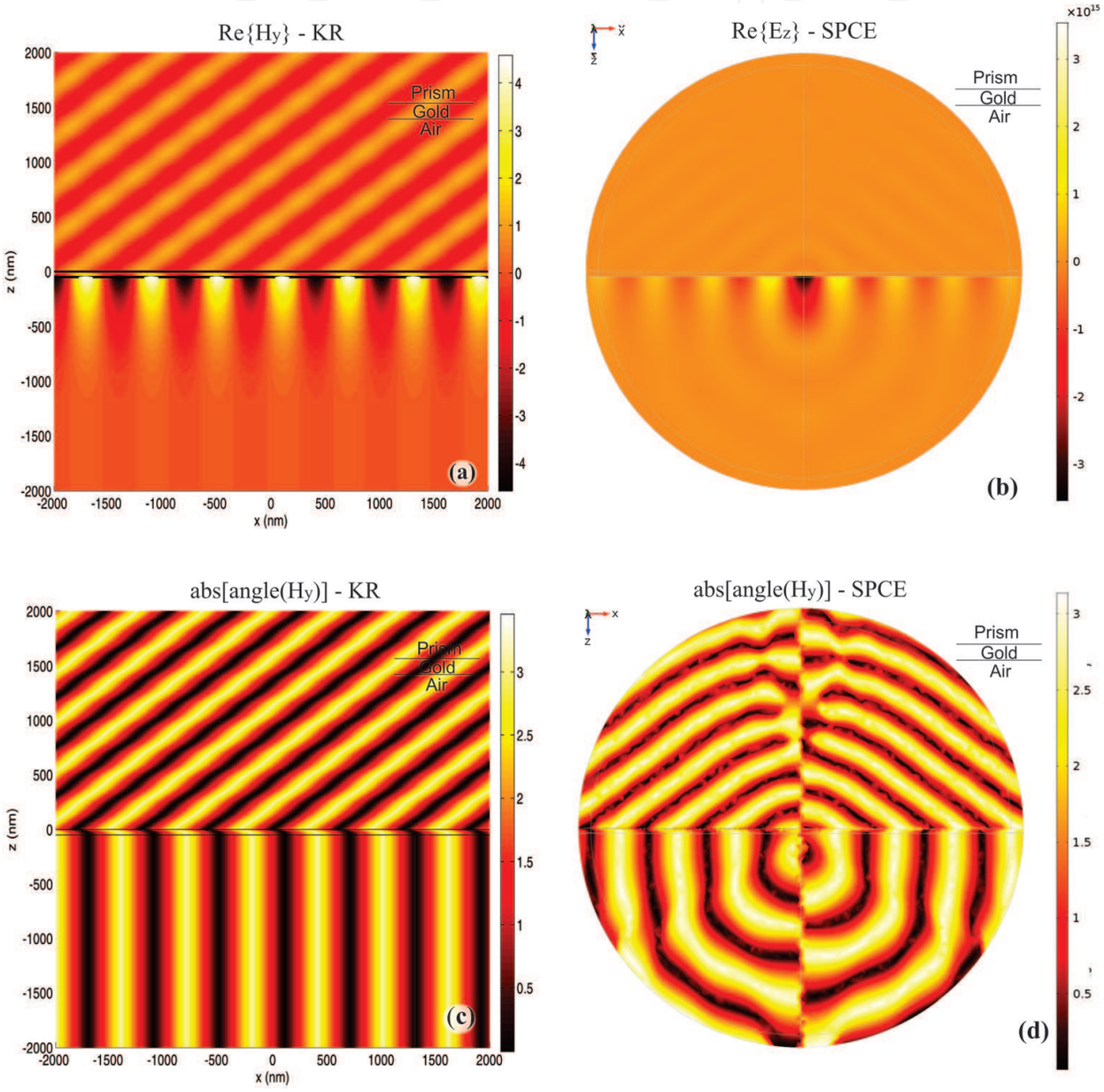

Figure 13. (a) Re(*Hy*) for plane wave incident with $\theta_{SPP} = 36.8163°$ obtained analytically for the sensor KR, (b) Re(E_z) for vertical dipole at z '= 20 nm for the sensor SPCE, (c) Angle of *Hy* obtained analytically for the KR sensor, (d) Angle of *Hy* obtained in the for the SPCE sensor.

describes the real part E_z field for the SPCE sensor with the source at $z' = 20$ nm. In **Figure 13(b)**, it is possible to observe the formation of surface plasma as a consequence of particle radiation above of the gold layer. Note that the z-axis was inverted only for reciprocal visualization. **Figure 13(c)** represents the phase of *Hy* obtained analytically for the KR sensor; it is possible to identify the incident phase of the plane wave on the gold layer.

Figure 13(d) illustrates the *Hy* phase obtained for the SPCE sensor. Note that, in the prism layer, magnetic transverse plane (TM) waves are obtained with the reciprocal phase of the KR sensor phase. The appearance of this polarized wave in the TM mode is explained because part of the emitter's optical emission is naturally in the TM mode and excites an SPP wave on the air/gold surface; then, after the evanescent wave passes through the thin metallic layer, it will radiate in the prism as a polarized propagation wave in TM mode.

So, a coupling angle was set on the SPCE sensor equal to the angle of plasma resonance occurred at the KR sensor, which was actually found $\theta_{SPCE} = 34.8° \approx \theta_{KR} = 36.8°$. It was observed that a gradual increase in the discretization of the meshes used to represent the dipole approximates the coupling angle of the SPCE sensor of the angle of resonance of the KR sensor, which in fact proves its electromagnetic reciprocity between the plasmonic modes of the KR and SPCE sensor.

4. Conclusion

In this article was presented a theoretical analysis of an SPR sensor in Kretschmann (KR) and SPCE configurations, when a periodic array of core-shell nanoparticles (CSNps) is immobilized on the sensor sensitive surface. For the SPR sensor in KR configuration, the CSNps array has approximated by an effective homogeneous layer to treat the resultant structure as a planar multilayer, which improved the computational processing. For the SPCE configuration, the CSNps array has been treated as equivalent dipoles and the study is performed by the discrete complex image method (DCIM).

The approximate model of the KR sensor was validated for low size of the CSNp, parameters a and b, and high distance d in the periodic array from the comparison with the numerical simulations using finite element method. We observed that the increase of the shell thickness tends to depress the validation of this approximate model, such as the metal-core radius, and the parameter d, instead, tends to improve the validation.

The modal analysis of the KR configuration reveled that, besides the SPP surface wave, multiples guide wave modes can be excited, even in TE polarization. The thickness of the SiO_2 layer can alter the order of these guide modes and for configured value guide wave modes of order 1 and 2 was observed. The characteristic field of the guide modes in TM polarization presents a surface wave in the gold-SiO_2 interface, such as the SPP wave. We observed better validation of the approximate model for the TE curves.

There are evidences, such as the higher field intensity in the CSNps array region, that can indicate a greater sensitivity response for the wave modes which the minimum point is closest

to the critical ATR angle. As the SiO_2 layer thickness can regulate the minimum point position, this parameter can also improve the sensor sensibility.

The sensitivity analysis revealed that both radius core and shell thickness increase the sensor response, but the radius core presented a greater influence in this behave, showing larger sensitivity to the parameter a. Because the dielectric shell reduces the sensor field interaction with the nanoparticles array, although this increases the size of the CSNps which, in general, intensifies the sensor response. The parameter d always tends to decrease the sensor response due to the reduction of the CSNps concentration in the array.

To develop the modal analysis of the SPCE sensor, we focus in the solution of the field equations for a resonant dipole over a multiple planar structure. The equations are optimized for direct application via DCIM method. The evaluation of the near field is presented and we observe that the waves radiated by the immobilized nanoparticles induce the surface plasmonic mode in the air-gold interface and radiating modes in the prism concentrated at specific angles.

The DCIM method was applied for a general solution of multilayer media using the generalized reflection coefficients. The far field results are presented by numerical simulations performed via finite element method and we observe that in SPCE configuration, the intensity of the lower lobes increases with the decrease in height z′. It is observed that the far field strength is greater for height $z' = 20$ nm.

By the last analysis of the sensor in the SPCE configuration, we demonstrated the reciprocity of the SPP modes in the configurations KR and SPCE. It has been found that the coupling angle of the SPP mode in the SPCE configuration is equal to the angle of maximum coupling of TM0 mode KR configuration.

Author details

Nadson Welkson Pereira de Souza[1,2], Jefferson Souza Costa[1], Rafael Correa dos Santos[1], André Felipe Souza da Cruz[1], Tommaso Del Rosso[3] and Karlo Queiroz da Costa[1]*

*Address all correspondence to: karlo@ufpa.br

1 Department of Electrical Engineering, Federal University of Para, Tucuruí-PA, Brazil

2 Department of Electrical Engineering, Federal University of South and Southeast of Para, Marabá-PA, Brazil

3 Department of Physics, Pontifical Catholic University of Rio de Janeiro, Rua Marques de São Vicente, Rio de Janeiro, Brazil

References

[1] Homola J. Surface plasmon resonance based sensors. In: Springer Series on Chemical Sensors and Biosensors: Methods and Applications. 4th ed. online ed. Springer; 2006. p. 33-44

[2] Wood RW. On a remarkable case of uneven distribution of light in a diffraction grating spectrum. Philosophical Magazine. 1902;**4**:396-402

[3] Wood RW. Diffraction gratings with controlled groove form and abnormal distribution of intensity. Philosophical Magazine. 1912;**23**:310-317

[4] Liedberg B, Nylander C, Lind T. Gas detection by means of surface plasmons. Sensors and Actuators. 1982;**3**:79-88

[5] Nylander C, Liedberg B, Lundstrom I. Surface plasmons resonance for gas detection and biosensing. Sensors and Actuators. 1983;**4**:299-304

[6] Chen Y, Chen JIL, Ginger DS. Plasmonic nanoparticle dimers for optical sensing of DNA in complex media. Journal of the American Chemical Society. 2010;**132**:9600-9601

[7] Feltis BN, Sexton BA, Glenn FL, Best MJ, Wilkins M, Davis TJ. A hand-held surface plasmon resonance biosensor for the detection of ricin and other biological agents. Biosensors and Bioelectronics. 2008;**23**:1131-1136

[8] Lindquist N, Nagpal P, McPeak KM, Norris DJ, Oh SH. Engineering metallic nanostructures for plasmonics and nanophotonics. Reports on Progress in Physics. 2012;**75**(75): 036501

[9] Cooper MA. Optical biosensors in drug discovery. Nature Reviews Drug Discovery. 2002;**1**:515-528

[10] Ignacy G, Lakowicz JR, Malicka J, Zygmunt G. Directional surface plasmon-coupled emission: A new method for high sensitivity detection. Biochemical and Biophysical Research Communications. 2003;**307**:435-439

[11] Cabrini S, Kawata S, editors. Nanofabrication Handbook. CRC Press; 2012

[12] Kaminow IP, Mammel WL, Weber HP. Metal-clad optical waveguides: Analytical and experimental study. Applied Optics. 1974;**13**:396-405

[13] Maier SA. Plasmonics: Fundamentals and Applications. 1st ed. New York: Springer; 2007

[14] Nguyen HH, Park J, Kang S, Kim M. Surface plasmon resonance: A versatile technique for biosensor applications. Sensors. 2015;**15**:10481

[15] Rosso TD, Sánchez JEH, Carvalho RDS, Pandoli O, Cremona M. Accurate and simultaneous measurement of thickness and refractive index of thermally evaporated thin organic films by surface plasmon resonance spectroscopy. Optics Express. 2014;**22**:18914-18923

[16] Mirabet LP. Synthesis, characterization and functionalization of metal and metal oxide nanoparticles. TEM microscopy study. [dissertation]. Barcelona: Universitat Autònoma de Barcelona; 2013

[17] da Costa KQ, Costa JS, Dmitriev V, Rosso TD, Pandoli O, Aucelio RQ. Analysis of surface plasmon resonance sensor coupled to periodic array of gold nanoparticles. In: Microwave and Optoelectronics; Nov 2015; SBMO/IEEE MTT-S International; 2015. pp. 1–5.

[18] Novotny L, Hecht B. Principles of Nano-Optics. 2nd ed. New York: Cambridge; 2012

[19] Choy T. Effective Medium Theory: Principles and Applications. 1st ed. Clarendon Press; 1999

[20] Kong JA. Electromagnetic Wave Theory. Massachusetts: Cambridge; 1998

[21] Ishimaru A. Electromagnetic Wave Propagation, Radiation and Scattering. New Jersey: Prentice Hall; 1991

[22] Chew W. Waves and Fields in Inhomogeneous Media. 1st ed. IEEE Press; 1996

[23] COMSOL Multiphysics 4.2a. COMSOL Inc. Available from: http://www.comsol.com./

[24] Sánchez JEH. Assembly of a surface plasmon resonance (SPR) spectrometer for the characterization of thin organic films [dissertation]. Rio de Janeiro-RJ, Brazil: Pontifícia Universidade Católica; 2013

[25] Costa JS, da Cruz AFS, dos Santos RC, da Costa KQ. Análise de um Sensor Plasmônico Acoplado à Arranjo Periódico de Nanopartículas tipo Core-Shell. In: Sociedade Brasileira de Telecomunicações (SBrT), editor. XXXIV Simpósio Brasileiro de Telecomunicações e Processamento de Sinais (SBrT 2016); Sep. 2016; Santarém-Pará-Brazil. 2016.

[26] Lakowicz JR. Radiative decay engineering: Surface plasmon-coupled directional emission. Analytical Biochemistry. 2004;153-169

[27] Ruckstuhl T, Enderlein J, Seeger S. Highly efficient optical detection of surface-generated fluorescence. Applied Optics. 1999;**38**

[28] Geddes M, Gryczynski L. Directional surface plasmon coupled emission. Journal of Fluorescence. 2004;**14**

[29] Jankowski D, Bojarski P, Kwiek P, Rangełowa JS. Donor–acceptor nonradiative energy transfer mediated by surface plasmons on ultrathin metallic films. Chemical Physics. 2010;**373**:238-242

[30] Lakowicz JR, Malicka J, Matveeva E, Gryczynski I, Gryczynski Z. Plasmonic technology: Novel approach to ultrasensitive immunoassays. Clinical Chemistry. 2005;**51**:1914-1922

[31] Tajdini MM, Mosallaei H. Characterization of Large Array of Plasmonic Nanoparticles on Layered Substrate: Dipole Mode Analysis Integrated with Complex Image Method. Applied EM and Optics Laboratory Northeastern University. Optical Society of America. 2011.

[32] Meng MT. Surface plasmon-coupled emission for applications in biomedical diagnostics. [thesis]. Glasnevin, Dublin, Irlanda: Dublin City University; 2009 Available from: http://doras.dcu.ie/14883/

[33] Kong JA, editor. Electromagnetic Wave Theory. John Wiley and Sons; 1986

[34] Aksun MI, Mittra R. Derivation of closed-form Green's functions for a general microstrip geometry. IEEE Transactions on Microwave Theory and Techniques. 1992;**40**

[35] Messa F, Boix RR, Medina F. Closed-form expressions of multilayered planar Green's functions that account for the continuous spectrum in the far field. IEEE Transactions on Microwave Theory and Techniques. 2008;**56**

[36] Zhuang L, Hu WY. Automatic incorporation of surface wave poles in discrete complex image method. Progress In Electromagnetics Research. 2008;**80**:161-178

[37] Simsek E, Liu J, Liu QH. A spectral integral method (SIM) for layered media. IEEE Transactions on Antennas and Propagation. 2006;**54**

[38] Aksum MI. A robust approach for the derivation of closed-form Green's. IEEE Transactions on Microwave Theory and Techniques. 1996;**44**